PROCEEDINGS OF SPIE

SPIEDigitalLibrary.org/conference-proceedings-of-spie

Magneto-optical studies of CdSe/CdMnS/CdS core/multi-shell colloidal nanoplatelets

Athos Petrou, Thomas A. Scrace, Joseph R. Murphy, Peiyao Zhang, Tenzin Norden, et al.

Athos Petrou, Thomas A. Scrace, Joseph R. Murphy, Peiyao Zhang, Tenzin Norden, Tianmu Zhang, Tim Thomay, Alexander N. Cartwright, Savas Delikanli, Mehmet Zafer Akgul, Himli Volkan Demir, "Magneto-optical studies of CdSe/CdMnS/CdS core/multi-shell colloidal nanoplatelets," Proc. SPIE 9931, Spintronics IX, 99311W (4 November 2016); doi: 10.1117/12.2239725

SPIE.

Event: SPIE Nanoscience + Engineering, 2016, San Diego, California, United States

Magneto-optical studies of CdSe/CdMnS/CdS core/multi-shell colloidal nanoplatelets

Athos Petrou[1,a], Thomas A. Scrace[a], Joseph R. Murphy[a], Peiyao Zhang[a], Tenzin Norden[a], Tianmu Zhang[a], Tim Thomay[a], Alexander N. Cartwright[a], Savas Delikanli[b,c], Mehmet Zafer Akgul[b,c], Hilmi Volkan Demir[b,c]

[a]State University of New York, University at Buffalo, 239 Fronczak Hall, Buffalo, NY, 14260; [b]Bilkent University (Turkey); [c]Nanyang Technological University (Singapore)

ABSTRACT

We studied the photoluminescence (PL) from CdSe/CdMnS/CdS core/multi-shell colloidal nanoplatelets, a versatile platform to study the interplay of optical properties and nanomagnetism. The photoluminescence (PL) exhibits σ+ polarization in the applied magnetic field. Our measurement detects the presence of even a single magnetic monolayer shell. The PL consists of a higher and a lower energy component; the latter exhibits a circular polarization peak. The time-resolved PL (trPL) shows a red shift as function of time delay. At early (later) times the trPL spectra coincide with the high (low) energy PL component. A model is proposed to interpret these results.

Keywords: nanoplatelets, diluted magnetic semiconductors, sp-d exchange interaction, core/shell, photoluminescence, time-resolved spectroscopy, magneto-optical spectroscopy

1. INTRODUCTION

Semiconductor nanocrystals exhibit characteristics that are strongly dependent on both their composition and size [1]. During the last 40 years, 2D structures were grown as quantum wells by either using molecular beam epitaxy (MBE) [2] or chemical vapor deposition (CVD) [3] techniques; in contrast, the 2D structures discussed in this paper are grown using solution-based methods. These colloidal quantum wells, or nanoplatelets (NPLs), are synthesized with a thickness control at the monolayer (ML) level and with lateral dimensions that are large compared to the de Broglie wavelength so that quantum confinement effects are negligible in the lateral plane. Single material nanoplatelet core structures using a variety of II-VI semiconductor materials have been synthesized by several groups[4-8]; nanoplatelet heterostructures have also been successfully synthesized[9-12]. Zero-dimensional colloidal nanocrystals differ from colloidal nanoplatelets as follows: (a) NPL emission is spectrally narrower[13] but still tunable[14], (b) NPLs have reduced fluorescence blinking[12], and (c) NPLs exhibit high photoluminescence quantum yields[13].

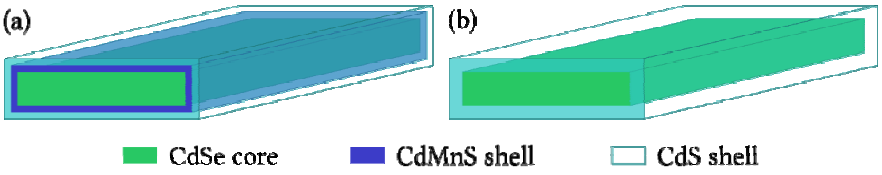

Figure 1: Schematic diagram of a core/multi-shell NPL structure with a CdSe core followed by a single monolayer shell of CdMnS and terminating with a monolayer of CdS (a) and a CdSe core followed by a shell of two monolayers of CdS (b).

2. METHODS

2.1 Samples

The nanoplatelets used in this study are synthesized such that the thickness, normal to the NPL plane (*z*-axis), is highly controlled while the lateral size (*x*- and *y*-axes) distribution is reasonably uniform[15]. The dimensions along the *z*-axis in

[1] petrou@buffalo.edu; phone: (716) 645-8183; www.acsu.buffalo.edu/~petrou/

Spintronics IX, edited by Henri-Jean Drouhin, Jean-Eric Wegrowe, Manijeh Razeghi, Proc. of SPIE
Vol. 9931, 99311W · © 2016 SPIE · CCC code: 0277-786X/16/$18 · doi: 10.1117/12.2239725

NPLs are comparable to those of QWs grown by conventional epitaxial methods and therefore the former exhibit similar confinement effects as the latter. The confinement in the *z*-direction in NPLs allows for the tailoring of photon emission characteristics by controlling the number of monolayers in each platelet; this is analogous to the way that the optical properties of colloidal quantum dots are controlled by adjusting their size[16]. Nanoplatelets are synthesized colloidally by preparing a NPL solution in a way similar to that used for colloidal quantum dots; details of the synthesis of these NPLs are given by Delikanli et. al.[17]. Magnetic ions (in our case, manganese) can be introduced into the layers of our II-VI based NPLs to explore the effects of *sp-d* exchange interactions between the spins of the carriers and those of the magnetic ions[17]. The effects of exchange interactions can be tailored through the precise control of both the heterostructure composition and the dimensions (confinement and lateral). Wave function engineering is achieved by: (a) control of the thickness of the component layers or (b) the deposition of one or more magnetic layers. Through structural design, the overlap of the carrier wave functions with the magnetic regions can be controlled so that the NPLs exhibit specific magneto-optical properties, such as PL circular polarization and Zeeman splitting.

Table 1: List of samples used in this study, the values in parentheses indicate the number of monolayers along the z-axis of the NPLs.

Sample	Composition
1	CdSe (5) / CdMnS (2) / CdS (2)
2	CdSe (3) / CdMnS (2) / CdS (2)
3	CdSe (5) / CdS (2)

The samples discussed in this paper, summarized in table 1, were fabricated according to the procedure described by Delikanli et. al.[17] by first synthesizing the NPL cores and enveloping this core with successive shell layers using colloidal atomic layer deposition (c-ALD). In this work, core/shell NPL structures were prepared by performing c-ALD deposition on either 5 ML (sample 1, sample 3) or 3 ML (sample 2) seed CdSe cores. During the c-ALD deposition, each side of the CdSe core surface was coated with 1 ML of shell material (either $Cd_{0.985}Mn_{0.015}S$ or CdS); as a result, for each cycle of shell growth, a total thickness of 2 MLs was deposited (1 ML on each of the top and bottom surfaces). A schematic of the NPL heterostructures used in this work is shown Figure 1. Non-magnetic sample 3 was used as a reference sample for the magnetic samples 1 and 2. The latter were studied for the investigation of exchange interactions between the spins of Mn^{2+} ions and those of the carriers.

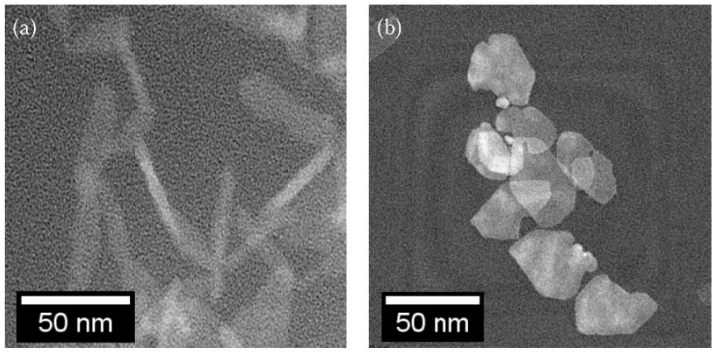

Figure 2: High-angle annular dark-field transmission electron microscopy (HAADF-TEM) images of sample 1 (a), and sample 2 (b).

High-angle annular dark-field transmission electron microscopy (HAADF-TEM) images of magnetic samples 1 and 2, are shown in panels of (a) and (b) of figure 2. The 5 ML CdSe seed NPLs used as cores of sample 1 exhibit regular rectangular shapes with average lateral dimensions of 55 ± 6 nm × 10 ± 2 nm. The dimensions of the 3 ML CdSe cores of sample 2, on the other hand, are difficult to determine as they tend to fold and have more irregular shapes. Manganese concentration of the magnetic shell layers in samples 1 and 2 was determined using energy-dispersive X-ray spectroscopy (EDS) measurements, assuming uniform manganese ion distribution with each CdMnS shell.

2.2 Experimental Methods

For the PL and magneto-PL measurements, the NPLs were excited using the linearly polarized output of a solid state laser emitting at 405 nm with a maximum power density of 0.2 W/cm^2. The experiments were conducted in the Faraday geometry in which the applied magnetic field is parallel to the direction of the emitted light. The PL was analyzed into its σ_+ (left circularly polarized) and σ_- (right circularly polarized) components using a combination of a quarter-wave plate and linear analyzer placed before the spectrometer entrance slit.

3. RESULTS

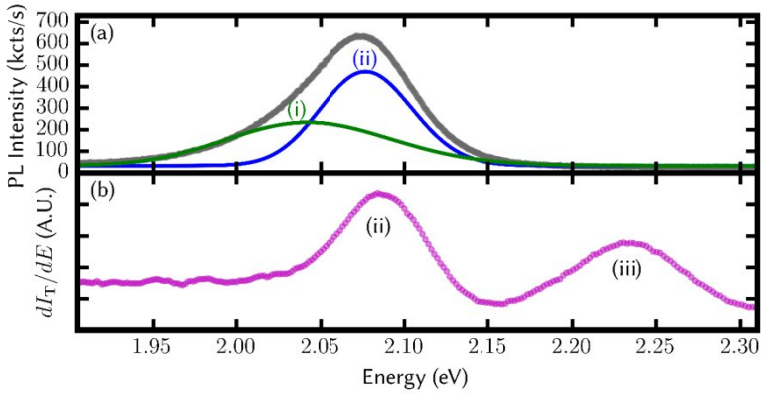

Figure 3: (a) The zero-field PL spectra of the magnetic sample is shown as grey points, result of fitting this data to two Gaussian functions that represent a low-energy (green line) and a high-energy (blue line) component are indicated by (i) and (ii), respectively. (b) The corresponding derivative of the transmission data is shown in magenta points with features (ii) also marked, the highest energy transmission feature (iii) is attributed to recombination involving light holes.

In the upper panel of figure 3 we show the zero-field PL spectrum from sample 1 (grey points) recorded at T = 10 K. The spectrum has a pronounced asymmetry on the low-energy side; for this reason, it was fit to the sum of two Gaussian functions centered at 2.036 meV and 2.077 meV [18]. We use a green (blue) line to indicate the low-energy (i) (high-energy (ii)) feature. To probe the origin of these features, we have also recorded the transmission spectrum under the same conditions. In figure 3b we plot the spectral derivative of the transmitted intensity as a function of photon energy. This spectrum has two distinct features: feature (ii) at 2.036 eV coincides with the corresponding PL feature and feature (iii) at 2.233 eV; this feature has been identified as the excitonic transition involving the first confinement light hole subband[17]. We note that PL feature (i) has no corresponding signature in the transmission spectrum. From the comparison of panels (a) and (b) in figure 3, we attribute feature (ii) to an excitonic transition that involves the lowest heavy hole subband and PL feature (i), having no corresponding feature in the transmission spectrum, to non-excitonic transitions.

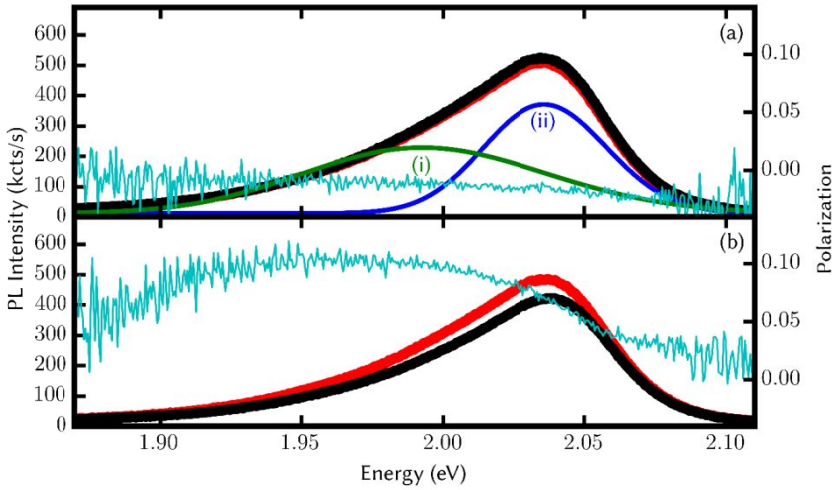

Figure 4: PL spectra from magnetic sample 1 using an excitation wavelength of 405 nm at a temperature of 7 K. The red (black) points indicate $\sigma_+(\sigma_-)$ circularly polarized PL components. The cyan line is the calculated circular polarization. In the upper panel, the applied magnetic field is 0 T and in the lower panel it is 7 T. The green and blue lines in panel (a) are the result of a fitting that uses two Gaussian functions to the asymmetric PL spectra.

In figure 4a (4b) we show the two circularly polarized PL components from sample 1 at $B = 0$ T ($B = 7$ T) recorded at 7 K. Red points indicate the σ_+ (LCP) PL component, while the black points denote the σ_- (RCP) PL component. The circular polarization at a particular photon energy is given by $P = (I_+\text{-}I_-)/(I_+\text{+}I_-)$ where $I_+(I_-)$ is the intensity of the σ_+ (σ_-) PL component. The spectral dependence of the calculated circular polarization is shown as the cyan lines. The asymmetric shape of the PL emission persists in the presence of an applied magnetic field. The circular polarization P, which is near zero at zero-field, becomes positive as the applied magnetic field is increased, indicating the presence of exchange interaction between the spins of the carriers and those of the Mn^{2+} ions[19]. The polarization peak in figure 4b has a maximum that coincides with the intensity maximum of feature (i) which indicates that the corresponding recombination occurs in the vicinity of the manganese ions located in the CdMnS shells.

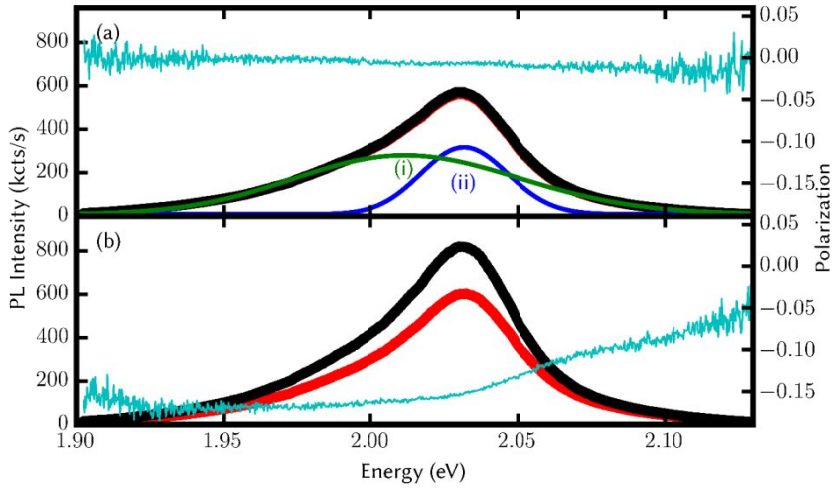

Figure 5: PL spectra from non-magnetic sample 3 using an excitation wavelength of 405 nm at a temperature of 7 K. The red (black) points indicate $\sigma_+(\sigma_-)$ circularly polarized PL components. The cyan line is the calculated circular polarization. In the upper panel, the applied magnetic field is 0 T and in the lower panel it is 7 T. The green and blue lines in panel (a) are the result of a fitting that uses two Gaussian functions to the asymmetric PL spectra.

The PL line asymmetry is also observed in the non-magnetic sample 3 as shown in figure 5. In figure 5a (5b) we show the two circularly polarized PL components at $B = 0$ T ($B = 7$ T) recorded at 7 K. Red points indicate the σ_+ (LCP) PL

component, while the black points denote the σ_- (RCP) PL component. The overall circular polarization of the PL emission from sample 3 is negative; furthermore, unlike sample 1, it is spectrally featureless.

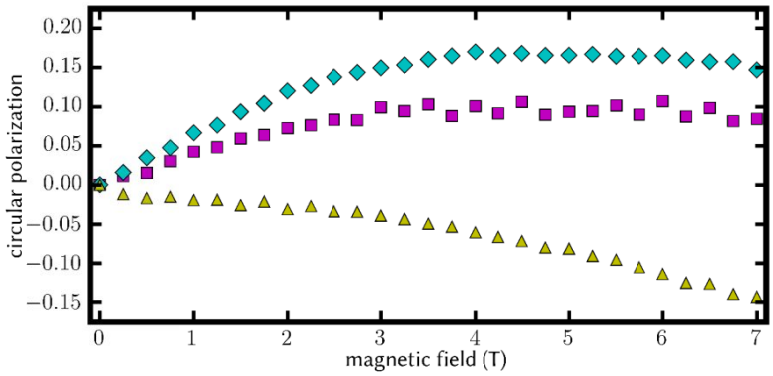

Figure 6: Circular polarization of PL plotted as a function of magnetic field at T = 7 K. Data for sample 1 is indicated by the magenta squares; sample 2 is indicated by cyan diamonds; and sample 3 is indicated by yellow triangles.

In figure 6 the net PL circular polarization, determined by spectrally integrating the intensities of the σ_+ and σ_- PL components, is plotted as a function of applied magnetic field at a temperature of 7 K. For magnetic samples 1 (magenta squares) and 2 (cyan diamonds), P initially increases with field and saturates before 4 T. In the data of sample 2, the polarization saturation value is larger than that of sample 1 due to increased carrier wave function overlap with the CdMnS shell[17]. The polarization saturation values of both samples 1 and 2 decrease dramatically with increasing T and vanish by approximately 25 K. Since the circular polarization follows the same dependence on B and T as the magnetization we conclude that the CdMnS shells exhibit Brillouin paramagnetism[19]. The magnetic field dependence of the polarization for non-magnetic sample 3 (yellow triangles) is distinctly different from that of the magnetic samples. The circular polarization of sample 3 is negative and has a nearly linear dependence on magnetic field. The negative sign of the circular polarization for sample 3 is due to the intrinsic conduction and valence band g-factors of CdSe[20].

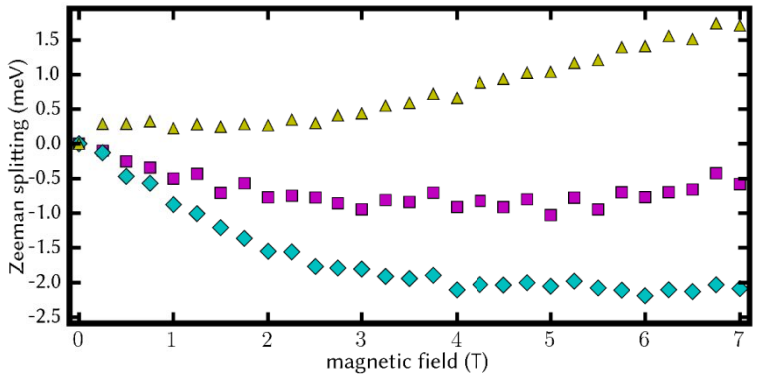

Figure 7: Zeeman splitting of PL plotted as a function of magnetic field at T = 7 K. Data for sample 1 is indicated by the magenta squares; sample 2 is indicated by cyan diamonds; and sample 3 is indicated by yellow triangles.

The origin of the PL circular polarization in magnetic samples 1 and 2 is due to the difference in the population distribution of the ±1/2 electrons and the ±3/2 holes among the conduction and valence band spin states. This population imbalance is due to the individual Zeeman splitting in the conduction and valence bands. The net Zeeman splitting, ΔE_Z, is defined as $\Delta E_Z = E_+ - E_-$ where $E_+(E_-)$ is the "center-of-mass" energy of the $\sigma_+(\sigma_-)$ PL component. The magnetic field dependence of ΔE_Z in figure 7 is similar to the dependence of P on B shown in figure 6. The algebraic sign of ΔE_Z as defined above, is compatible with the sign of the polarization; for magnetic samples 1 and 2, the σ_+ component has a lower energy than the σ_- component resulting in $I_+ > I_-$ and therefore positive circular polarization ($P > 0$). The opposite is true for the non-magnetic sample 3 where the σ_- component has a lower energy and thus $I_- > I_+$ resulting in negative circular polarization ($P < 0$).

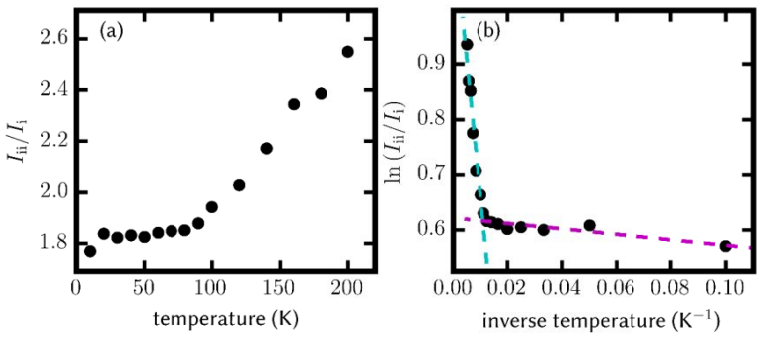

Figure 8: (a) The evolution of the ratio Iii/Ii as a function of temperature for sample 1 is indicated by the black points. (b) The value of ln(Iii/Ii) is plotted versus 1/T; here, Ii and Iii represent the respective fitted PL peak intensities. Two temperature regions are identified and linear fits to the high (low) temperature data are indicated by the cyan (magenta) dashed line.

The dependence of P and ΔE_Z on magnetic field and temperature for samples 1 and 2 shows the presence of exchange interactions between the carrier spins and those of the Mn^{2+} ions in the CdMnS shells. The intensity ratio I_{ii}/I_i of the two PL features identified in figure 3 is plotted as a function of temperature in figure 8a. This ratio changes little for temperatures between 10 K and 90 K; however, for the temperature region between 90 K and 200 K, this ratio increases sharply with increasing temperature. In figure 8b we plot the $\ln[I_{ii}/I_i]$ as a function of $1/T$; using the equation $\ln[I_{ii}/I_i] = -E_{loc}/k_BT$ we extract values of E_{loc}, the localization energy associated with the carriers involved in the recombination process of transition (i). For the low temperature region (10 K $\leq T \leq$ 90 K), the value of E_{loc} is very small, indicating the presence of a band of closely spaced energy levels. In contrast, E_{loc} in the high-temperature region (90 K $\leq T \leq$ 200 K) is equal to 4.2 meV.

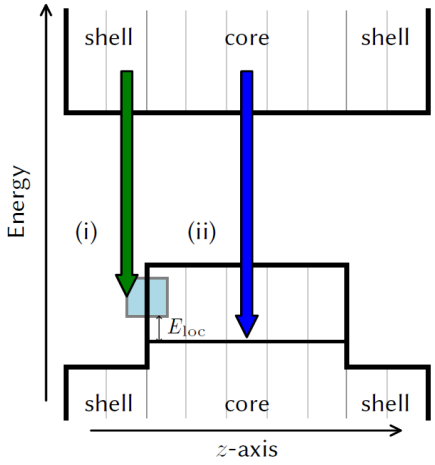

Figure 9: A diagram of the recombination scheme of our core/multi-shell nanoplatelet heterostructures. The vertical axis represents energy and the horizontal axis, the position along the z (vertical) dimension. The spacing between the grid of light grey lines indicates the thickness of single monolayers. The two proposed recombination channels are indicated by the green and blue arrows marked (i) and (ii) corresponding to the corresponding PL features identified in figure 3.

Based on the results of figure 8, we construct a model of the band structure and the recombination mechanisms associated with PL features (i) and (ii). As mentioned earlier, feature (ii) is excitonic in nature; feature (i) on the other hand involves recombination of delocalized electrons with hole states localized at the CdSe/CdMnS core/shell interfaces. This is strongly supported by the large positive circular polarization associated with feature (i) in magnetic samples 1 and 2 in the presence of an externally applied magnetic field. Given the fact that the exchange interaction between the spins of holes and the spins of Mn^{2+} ions is stronger (by a factor of 5) than the corresponding e-Mn^{2+} interaction [19], we

conclude that the localized carriers involved in the recombination process of feature (i) must be in the vicinity of the magnetic ions and that those carriers must be holes. The localization energy, E_{loc}, of the holes is equal to 4.2 meV as discussed above in connection to figure 8b. A possible source of the localized states band shown in figure 9 as the light blue region is the variation of the localized holes states energy in the *xy*-plane of the nanoplatelets at the core/shell interfaces.

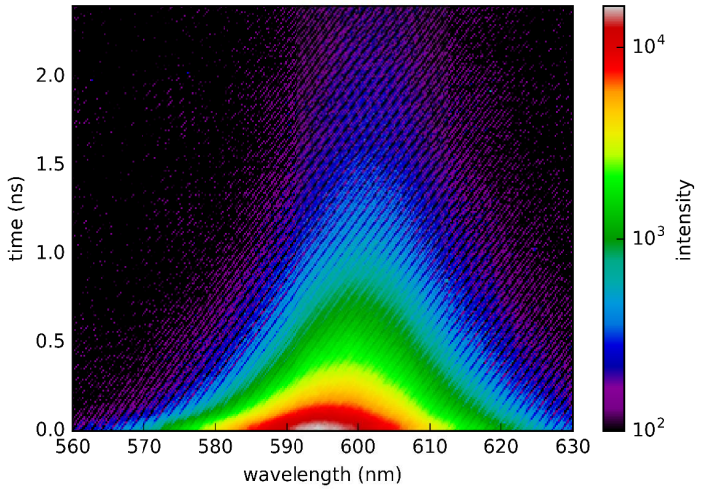

Figure 10: The intensity of the PL is represented by the color of this streak image, which is mapped in two dimensions; the horizontal axis corresponds to wavelength in nm and the vertical axis corresponds to the time delay as measured from the arrival of the excitation pulse.

To determine the origin of these two PL features, we studied the recombination dynamics in our samples using trPL spectroscopy and in figure 10 we show a 2D time-wavelength map of the PL intensity for the magnetic sample. For each time slice (δt = 10 ps), the spectra are fit to a Gaussian function; examples of these slices for the magnetic (non-magnetic) sample are shown in the inset of figure 11a (figure 11b). In these insets, the horizontal axis corresponds to energy in eV and the vertical is the normalized intensity. The spectra shown as insets correspond to times of 0 ns (blue points) and 3.5 ns (green points). We note that these trPL spectra do not exhibit the same degree of asymmetry as those of the PL.

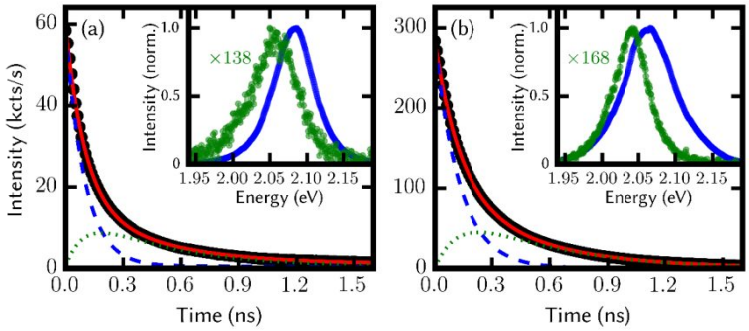

Figure 11: The temporal evolution of the PL intensity from the magnetic sample is shown in panel (a) and that of the non-magnetic sample is shown in panel (b) using black points. The calculated intensities of features (i) and (ii) are shown using dotted green and dashed blue lines, respectively. The sum of these intensities is indicated by red lines. The data of the insets represent time slices of the trPL spectra at $\Delta t = 0$ ns (blue points) and at $\Delta t = 3.5$ ns (green points). These inset spectra have been normalized and dark count-corrected so as to have the same peak intensity, and the green numbers indicate the magnification factor for the spectra at $\Delta t = 3.5$ ns.

The two PL emission components labeled (i) and (ii) in figure 3 correspond to the two distinct recombination channels shown in figure 9. An analysis using a bi-exponential decay function to fit the PL spectra assumes two independent processes, *i.e.*, with no inter-channel energy transfer. Instead, we constructed a rate equation-based model which

incorporated a coupling of the two processes. To simplify the solutions of these rate equations, make the following assumptions: First, the time resolution of the streak measurements in this study exceeds the excitation time of the carriers; therefore, we treat the excitation of electron-hole pairs to be instantaneous. While there is a finite timescale associated with excitation, it is substantially shorter than the resolution. Second, energy transfer occurs only from the high-energy channel (ii) to the low-energy channel (i); transfer in the opposite direction, *i.e.*, from (i) to (ii), is negligible because the energy difference of those two processes is much greater than $k_B T$, given the low temperature at which this experiment was conducted. And third, the result of photo-excitation is that primarily only channel (ii), which is excitonic, is initially populated and channel (i) is empty at $t = 0$. The latter becomes populated via energy transfer from channel (ii) as indicated in figure 13.

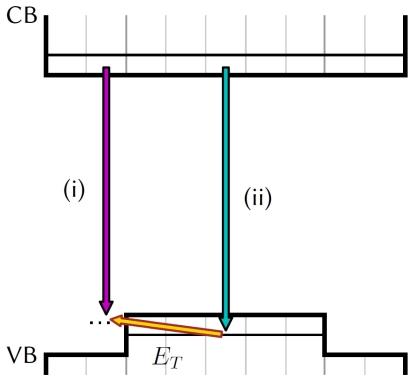

Figure 12: Schematic diagram of the recombination channels shown in figure 4. In this figure, we include the transfer of excitation from the excitonic channel (ii) to the interface-related channel (i) indicated by the yellow arrow.

Based on these assumptions, we construct the following system of coupled differential equations:

$$\frac{dN_{\mathrm{i}}(t)}{dt} = -\frac{N_{\mathrm{i}}(t)}{\beta_{\mathrm{i}}} + C\frac{N_{\mathrm{ii}}(t)}{\beta_{\mathrm{i}}} \tag{1}$$

$$\frac{dN_{\mathrm{ii}}(t)}{dt} = -\frac{N_{\mathrm{ii}}(t)}{\beta_{\mathrm{ii}}} \tag{2}$$

Here, $N_{\mathrm{i}}(t)$ is the number of carrier pairs at time t associated with channel (i), $N_{\mathrm{ii}}(t)$ is the number of excitons at time t associated with channel (ii), β_{i} is the lifetime associated with channel (i), β_{ii} is the lifetime associated with channel (ii), and C is a parameter that describes the coupling between the two channels.

The analytical solutions to this model are:

$$N_{\mathrm{i}}(t) = \frac{1}{\beta_{\mathrm{i}} - \beta_{\mathrm{ii}}}\left(\beta_{\mathrm{i}} N_{\mathrm{i}}(0)\, e^{-\frac{t}{\beta_{\mathrm{i}}}} - \beta_{\mathrm{ii}} N_{\mathrm{i}}(0)\, e^{-\frac{t}{\beta_{\mathrm{i}}}} + C\beta_{\mathrm{ii}} N_{\mathrm{ii}}(0)\, e^{-\frac{t}{\beta_{\mathrm{i}}}} - C\beta_{\mathrm{ii}} N_{\mathrm{ii}}(0)\, e^{-\frac{t}{\beta_{\mathrm{ii}}}}\right) \tag{3}$$

$$N_{\mathrm{ii}}(t) = N_{\mathrm{ii}}(0)\, e^{-\frac{t}{\beta_{\mathrm{ii}}}} \tag{4}$$

Using the assumption that the state associated with channel (i) is initially unpopulated, the solutions simplify to:

$$N_{\mathrm{i}}(t) = \frac{C\beta_{\mathrm{ii}} N_{\mathrm{ii}}(0)}{\beta_{\mathrm{i}} - \beta_{\mathrm{ii}}}\left(e^{-\frac{t}{\beta_{\mathrm{i}}}} - e^{-\frac{t}{\beta_{\mathrm{ii}}}}\right) \tag{5}$$

$$N_{\mathrm{ii}}(t) = N_{\mathrm{ii}}(0)\, e^{-\frac{t}{\beta_{\mathrm{ii}}}} \tag{6}$$

The value of $N_{\mathrm{ii}}(0)$ was set to the PL intensity at $t = 0$ and the remaining parameters: β_{i}, β_{ii} and C were used to fit these solutions to the experimentally obtained data. Values for β_{i} and β_{ii} were constrained to be non-negative and values of C were constrained to be within the interval [0,1].

The results of the fit for the magnetic (non-magnetic) sample are summarized in figure 11. In the main panels of figure 11a and 11b, we plot the following: calculated PL intensity of channel (i) using dotted green lines; calculated PL intensity of channel (ii) using dashed blue lines; calculated PL intensity of both channels using red lines (sum of green and blue lines); and the experimental PL intensities integrated over all recorded wavelengths using black points.

The resulting fit parameters are summarized in table 2.

Table 2: Fit parameters of the time-resolved PL intensity using the solutions of our rate equation model.

	Sample 1	**Sample 3**
β_i (ns)	0.422	0.449
β_{ii} (ns)	0.098	0.131
C	0.940	0.902

Our approach is to fit the solutions to the spectrally integrated intensity over all recorded wavelengths as shown in figure 11a and figure 11b. The difference in the values obtained for β_i and β_{ii} is compatible with the fact that channel (ii) is excitonic while channel (i) is due to recombination between free electrons with localized holes. We note that the values of the extracted lifetimes (in particular that of the slow process, (i)), while sensitive to the underlying assumptions, always result in two distinct timescales. Of the lifetimes associated with these processes the lower-energy process is significantly slower than that of the high-energy process. We identify the parameters β_i and β_{ii} listed in table 2 as the lifetimes associated with the respective channels.

4. CONCLUSIONS

We have studied the magneto photoluminescence of solution-grown nanoplatelets that consist of CdSe cores, followed by CdMnS shells and are terminated with CdS shells. In the presence of an externally applied magnetic field, the net PL emission becomes predominantly left circularly polarized (σ_+) indicating the presence of exchange interaction between the spins of the carriers and those of the Mn^{2+} ions. The sign of the Zeeman splitting is compatible with the circular polarization of the PL emission, *i.e.*, $E_+ < E_-$, where E_+ (E_-) is the energy associated with the recombination of -1/2 (+1/2) electrons with +3/2 (-3/2) holes. Both the circular polarization and the Zeeman splitting have a Brillouin-like dependence on magnetic field and temperature. The photoluminescence emission is asymmetric and can be decomposed into two Gaussian features. The circular polarization maximum coincides with the intensity peak of the low-energy feature. Using the Mn^{2+} ions as a marker, we identified this low-energy feature as due to recombination of delocalized electrons with holes localized at the CdSe/CdMnS interface. The high-energy feature is excitonic in nature and involves recombination of delocalized electrons with holes confined in the CdSe core. The presence of two distinct lifetimes, β_i and β_{ii}, determined from the analysis of trPL experimental results further support this suggested model.

ACKNOWLEDGEMENTS

The authors would like to thank EU-FP7 Nanophotonics4Energy NoE, and TUBITAK EEEAG 109E002, 109E004, 110E010, 110E217, and 112E183, and NRF-RF-2009-09, NRF-CRP-6-2010-02, and A*STAR of Singapore for the financial support. H.V.D. acknowledges support from ESF-EURYI and TUBA-GEBIP. Work at the University at Buffalo was supported by NSF DMR 1305770.

REFERENCES

[1] A. P. Alivisatos, "Perspectives on the Physical Chemistry of Semiconductor Nanocrystals," The Journal of Physical Chemistry, 100(31), 13226-13239 (1996).

[2] R. Dingle, [Confined carrier quantum states in ultrathin semiconductor heterostructures] Springer Berlin Heidelberg, (1975).

[3] R. D. Dupuis, P. D. Dapkus, N. Holonyak *et al.*, "Room-temperature laser operation of quantum-well Ga(1−x)AlxAs-GaAs laser diodes grown by metalorganic chemical vapor deposition," Applied Physics Letters, 32(5), 295-297 (1978).

[4] S. Ithurria, and B. Dubertret, "Quasi 2D Colloidal CdSe Platelets with Thicknesses Controlled at the Atomic Level," Journal of the American Chemical Society, 130(49), 16504-16505 (2008).

[5] S. Ithurria, M. D. Tessier, B. Mahler *et al.*, "Colloidal nanoplatelets with two-dimensional electronic structure," Nature Materials, 10(12), 936-941 (2011).

[6] J. Joo, J. S. Son, S. G. Kwon *et al.*, "Low-Temperature Solution-Phase Synthesis of Quantum Well Structured CdSe Nanoribbons," Journal of the American Chemical Society, 128(17), 5632-5633 (2006).

[7] Z. Li, H. Qin, D. Guzun *et al.*, "Uniform thickness and colloidal-stable CdS quantum disks with tunable thickness: Synthesis and properties," Nano Research, 5(5), 337-351 (2012).

[8] C. Schliehe, B. H. Juarez, M. Pelletier *et al.*, "Ultrathin PbS Sheets by Two-Dimensional Oriented Attachment," Science, 329(5991), 550-553 (2010).

[9] S. Ithurria, and D. V. Talapin, "Colloidal Atomic Layer Deposition (c-ALD) using Self-Limiting Reactions at Nanocrystal Surface Coupled to Phase Transfer between Polar and Nonpolar Media," Journal of the American Chemical Society, 134(45), 18585-18590 (2012).

[10] Y. Kelestemur, M. Olutas, S. Delikanli *et al.*, "Type-II Colloidal Quantum Wells: CdSe/CdTe Core/Crown Heteronanoplatelets," The Journal of Physical Chemistry C, 119(4), 2177-2185 (2015).

[11] B. Mahler, B. Nadal, C. Bouet *et al.*, "Core/Shell Colloidal Semiconductor Nanoplatelets," Journal of the American Chemical Society, 134(45), 18591-18598 (2012).

[12] M. D. Tessier, P. Spinicelli, D. Dupont *et al.*, "Efficient Exciton Concentrators Built from Colloidal Core/Crown CdSe/CdS Semiconductor Nanoplatelets," Nano Letters, 14(1), 207-213 (2014).

[13] M. D. Tessier, B. Mahler, B. Nadal *et al.*, "Spectroscopy of Colloidal Semiconductor Core/Shell Nanoplatelets with High Quantum Yield," Nano Letters, 13(7), 3321-3328 (2013).

[14] S. Delikanli, B. Guzelturk, P. L. Hernandez-Martinez *et al.*, "Continuously Tunable Emission in Inverted Type-I CdS/CdSe Core/Crown Semiconductor Nanoplatelets," Advanced Functional Materials, 25(27), 4282-4289 (2015).

[15] B. Guzelturk, M. Olutas, S. Delikanli *et al.*, "Nonradiative energy transfer in colloidal CdSe nanoplatelet films," Nanoscale, 7, 2545-2551 (2015).

[16] C. B. Murray, D. J. Norris, and M. G. Bawendi, "Synthesis and characterization of nearly monodisperse CdE (E = sulfur, selenium, tellurium) semiconductor nanocrystallites," Journal of the American Chemical Society, 115(19), 8706-8715 (1993).

[17] S. Delikanli, M. Z. Akgul, J. R. Murphy *et al.*, "Mn2+-Doped CdSe/CdS Core/Multishell Colloidal Quantum Wells Enabling Tunable Carrier-Dopant Exchange Interactions," Acs Nano, 0(ja), null-null (2015).

[18] J. R. Murphy, S. Delikanli, T. Scrace *et al.*, "Time-resolved photoluminescence study of CdSe/CdMnS/CdS core/multi-shell nanoplatelets," Applied Physics Letters, 108(24), 242406 (2016).

[19] J. K. Furdyna, "Diluted magnetic semiconductors," Journal of Applied Physics, 64(4), R29-R64 (1988).

[20] G. Long, B. Barman, S. Delikanli *et al.*, "Carrier-dopant exchange interactions in Mn-doped PbS colloidal quantum dots," Applied Physics Letters, 101(6), 062410-062410 (2012).